Differential optical spatial modulation with pulse position modulation over atmospheric turbulence

Huiqin Wang,* Mao Yicong, Yue Zhang, Cao Minghua, Wang Chanfei, and Bao Zhongxian
Lanzhou University of Technology, School of Computer and Communication, Lanzhou, China

Abstract. Optical spatial modulation (OSM), a recent optical multiple-input multiple-output transmission scheme in wireless optical communication, has aroused great research interests. OSM scheme requires accurate channel state information (CSI) during transmitter and receiver sides, but it is difficult to accurately estimate CSI in OSM scheme. Therefore, a scheme named differential optical spatial modulation scheme with pulse position modulation (DOSM-PPM) based on the space-time mapping block of orthogonal design is proposed in order to completely avoid CSI estimation. The bit error rate (BER) performance of DOSM-PPM is analyzed under log-normal turbulent channel model and simulated using Monte Carlo method. The results show that the transmission rate of DOSM-PPM is improved effectively. Meantime, the proposed DOSM-PPM scheme outperforms DOSM scheme with spatial pulse amplitude modulation by 1 dB at 1×10^{-3} BER with the same spectrum efficiency. © *2020 Society of Photo-Optical Instrumentation Engineers (SPIE)* [DOI: 10.1117/1.OE.59.9.096109]

Keywords: wireless optical communication; optical spatial modulation; differential optical spatial modulation; pulse position modulation; bit error rate.

Paper 20200503 received Apr. 29, 2020; accepted for publication Sep. 10, 2020; published online Sep. 30, 2020.

1 Introduction

With the growing demand for terminal numbers and data service, we have higher requirements of the transmission rate of the backbone and access network. Wireless optical communication (WOC), a novel access network technology, has sparked interest in the field due to its high transmission rate, inherent security, high bandwidth, and ease of installation.[1] Despite these advantages, transmission performance of WOC system is negatively affected by fading link of scattering and scintillation.[2] In order to minimize the impact of the atmospheric turbulence (AT), optical multiple-input multiple-output (MIMO) has been proposed.[3] However, multiple lasers in traditional optical MIMO system are simultaneously activated, which leads to interchannel interference (ICI) and interantenna synchronization (IAS).[4] These weaknesses limit the development and application of optical MIMO schemes.

Optical spatial modulation (OSM) scheme is a novel optical MIMO scheme where only one laser is activated at any interval, thereby completely avoiding the ICI and IAS among lasers at transmitter (Tx) side.[5] OSM scheme transmits simultaneously information across both the signal and space domain. In other words, one part of incoming bits is used to select an index of lasers in space domain while the rest is mapped onto the selected laser using the digital modulation.[6] OSM scheme, compared with the traditional optical MIMO scheme, improves transmission rates through transmitting extra bits information by means of laser indices. Optical space shift keying (OSSK) is a special scheme simpler than OSM scheme, which transmits information only through the laser index. The theoretical analysis and experiments about OSM/OSSK scheme are explored in Refs. 7–17. Pulse position modulation (PPM) and pulse amplitude modulation (PAM) are used for OSM system in Refs. 7 and 8, respectively. Error performance and energy efficiency are enhanced by utilizing PPM in Ref. 7, whereas spectrum efficiency (SE) is

*Address all correspondence to Huiqin Wang, E-mail: whq1222@lut.cn

improved using PAM in Ref. 8. Pham et al.[9] investigate the influence of spatial pulse position modulation (SPPM) on link performance under atmospheric laser communication, such as geometric expansion, turbulence, and pointing error (PE). Spatial pulse position amplitude modulation scheme is proposed by combining OSM with high-dimensional PPAM to balance SE and error performance in Ref. 10. Expression of theoretical channel capacity and probability density function (PDF) of average bit error rate (ABER) over log-normal, negative exponential (NE) and gamma–gamma channels model in OSSK scheme are investigated in Refs. 11–16.

The above OSM schemes are based on an assumption that the receiver (Rx) can obtain accurate channel state information (CSI). When the channel changes more slowly than transmission rate, the assumption is established. However, the fast change of channel leads to unstable CSI in the rapid change scenario, such as in underwater optical communication and atmospheric laser communication. It is difficult to accurately estimate CSI in actual communication systems because of the time-varying and complexity of the channel. Especially, when the number of simultaneous activated lasers is large, the channel estimation is very complex. In MIMO schemes, the CSI estimation is avoided in differential modulation system, such as differential Alamouti scheme and differential spatial multiplexing.[17,18] Recently, with the development of technology, the differential spatial modulation (DSM) is proposed on the basis of the combination of differential technology and spatial modulation.

DSM scheme originated from radio frequency (RF). In the field of RF, DSM with pulse phase modulation is proposed for the first time.[19] Based on this research, DSM scheme of RF field is optimized and improved in Refs. 20–24. Unfortunately, DSM in the RF domain is not directly applicable to WOC systems. Therefore, a differential optical spatial modulation (DOSM) scheme is introduced into WOC system for the first time in Ref. 25, in which DOSM scheme with PAM (DOSM-PAM) and differential optical space shift keying (DOSSK) scheme are proposed, and the average symbol error rate of four-levels DOSM-PAM is derived over gamma–gamma and NE channel model. The DOSM scheme[25] adopts diversity technology to improve transmission reliability. That is, all the activated lasers transmit the same bit information in a transmission matrix block. In addition, the use of the PAM further increases SE of DOSM scheme.

Intensity modulation and direct detection (IM/DD) schemes are used in most of the WOC system.[26] PAM improves the SE, but increasing the PAM order comes at the cost of a higher peak-to-power ratio. The high peak-to-power ratio causes the Tx to operate in the nonlinear region.[10] Compared to PAM, PPM is a popular intensity modulation because of its higher energy efficiency, inherent orthogonality, and needless adaptive threshold.[27,28] In this paper, we propose an DOSM scheme based on PPM and space-time block coding.[29,30] First, the difference design is realized by space-time coding block to avoid CSI estimation. Second, PPM is employed to enhance error performance and energy efficiency. Finally, we adopt multiplexing technology to transmit the different bit information on all the activated lasers, maximizing the transmission rate of DOSM scheme.

The remainder of this paper is organized as follows. Section 2 presents the system model of our proposed DOSM. In Sec. 3, we derive the average BER of our proposed $n_t = 2$ DOSM-2PPM scheme. Theoretical and Monte Carlo simulation results are presented in Sec. 4. Conclusion and future work are included in Sec. 5.

2 System Model

We consider an $n_r \times n_t$ DOSM-PPM scheme, as is shown in Fig. 1, where n_t and n_r are the numbers of lasers (LD) at Tx and photodetectors (PD) at Rx, respectively. At the Tx side, incoming random bitstream is divided into DOSM's bit blocks with $\lfloor \log_2(n_t!) \rfloor + n_t \log_2(L) = m$ bits, where $\lfloor \cdot \rfloor$ denotes the floor function, L stands for PPM order. The incoming data bits m are made up of two groups. The first group containing $\lfloor \log_2(n_t!) \rfloor$ bits is used to select the index of the lasers in space domain, that is, the spatial constellation point is represented by one transmission block. The other group with $n_t \log_2(L)$ bits mapped on n_t lasers by means of L-PPM constellation, respectively. A unique space-time mapping block $\mathbf{X}$ is generated using these m bits. At t'th transmission block, the current actual transmitted block $\mathbf{S}_t$ is generated by utilizing the previous transmitted block $\mathbf{S}_{t-1}$ and the current space-time mapping block $\mathbf{X}_t$ as

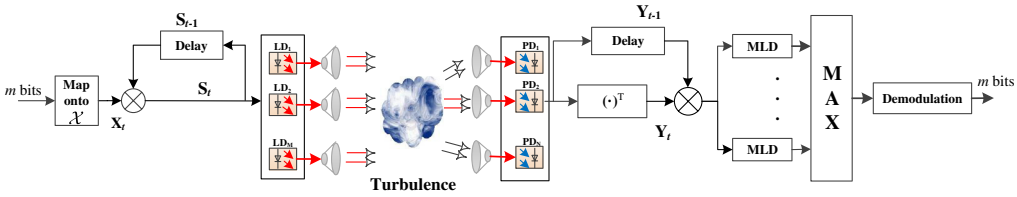

Fig. 1 DOSM-PPM scheme model.

$$\mathbf{S}_t = \mathbf{S}_{t-1}\mathbf{X}_t. \tag{1}$$

$\mathbf{S}_t$ and $\mathbf{X}_t$ are described in Secs. 2.1 and 2.2, respectively. The differential scheme satisfies the following theorem.[19]

Theorem 1. Consider a DOSM scheme with n_t lasers, transmitted block set $\mathcal{S}$ and space-time mapping block set $\mathcal{X}$, where $\mathcal{S}$ and $\mathcal{X}$ denote all possible results of the transmitted block and space-time mapping block, respectively. The set $\mathcal{S}$ and $\mathcal{X}$ with n_t lasers and L-PPM constellation contain $n_t!L^{n_t}$ blocks. For any $n \geq n_t$, $n \times n$ space-time mapping block $\mathbf{X} \in \mathcal{X}$ ($\mathbf{X}\mathbf{X}^{\mathrm{T}} = \mathbf{X}^{\mathrm{T}}\mathbf{X} = \mathbf{I}$, $\mathbf{I}$ is the identity matrix and $(\cdot)^{\mathrm{T}}$ is the transpose operation.) and $n_t \times n$ transmitted matrices of $\mathbf{S} \in \mathcal{S}$ satisfy $\mathbf{S}\mathbf{X} \in \mathcal{S}$.

Before the Tx side begins the transmission process, an $n_t \times (n_t L)$ known initialized matrix $\mathbf{S}_0$ is transmitted. The transmitted optical signal through the atmospheric turbulent channel is transmitted by the laser and received by PDs. Then the original data bits are recovered by the maximum likelihood sequence detection (MLSD) algorithm at Rx side.

2.1 *Actual Transmitted DOSM Block S*

In the traditional OSM scheme, only one laser is activated at a certain symbol period thus the $n_t \times 1$ signal vector can be expressed as $\mathbf{s} = [0, \ldots, 0, s_{n_t}, 0, \ldots, 0]^{\mathrm{T}}$, where only the n_t'th element is nonzero. In the proposed DOSM-PPM scheme, the transmitted matrix $\mathbf{S}$ is formed by employing the traditional $n_t \times 1$ OSM vector over n_t symbol periods. This means that each transmitted matrix is transmitted during n_t symbol periods. Then the DOSM's transmitted block is $\mathbf{S} = [\mathbf{s}_1; \mathbf{s}_2; \ldots; \mathbf{s}_{n_t}]$, where $\mathbf{s}_i (i = 1,2, \ldots, n_t)$ is one of the possible OSM constellation vectors. $\mathbf{S}$ is an $n_t \times n_t$ matrix and satisfies following conditions.[19]

(1) Only one laser is activated in each symbol period, that is, there is only one nonzero element in each column.
(2) In a transmitted matrix $\mathbf{S}$ with n_t continuous symbol periods, each laser is activated only once, that is, each row has only one nonzero element.

According to the above two properties, $n_t!$ different structures with orthogonality are generated. $\lfloor \log_2(n_t!) \rfloor$ bits are used to select $2^{\log_2(n_t!)}$ distinct structures as transmitted block $\mathbf{S}$. L-PPM constellation is utilized on each activated laser, and each symbol period is divided into L slots. That is, one of the slots in each symbol period is activated. Therefore, a block $\mathbf{S}$ of DOSM scheme with L-PPM modulation is expanded to an $n_t \times (n_t L)$ matrix.

For example, a transmitted block is given by $\mathbf{S} = \begin{bmatrix} 0 & s_{12} \\ s_{21} & 0 \end{bmatrix}$ for $n_t = 2$ DOSM scheme, which means that at symbol period 1, the symbol s_{21} is transmitted from laser 2, whereas another laser remains idle. At symbol period 2, the symbol s_{12} is transmitted from laser 1, whereas another laser remains idle. Assume that s_{21} and s_{12} employ 2-PPM constellation, each of symbol period is divided into two time slots. Only one slot is activated in any symbol period.

2.2 *Differential Encoding Processing*

The space-time mapping block $\mathbf{X}$ is one of the key problems to perform differential operation. The space-time mapping block to be designed must satisfy orthogonality. Considering a

Table 1 Space-time mapping block X of DOSM scheme with $n_t = 2$ and 2-PPM.

Input m bits	Laser indices	Λ_1	Λ_2	X	Input m bits	Laser indices	Λ_1	Λ_2	X
000	(1,2)	$\begin{bmatrix}1&0\\0&1\end{bmatrix}$	$\begin{bmatrix}1&0\\0&1\end{bmatrix}$	$\begin{bmatrix}1&0&0&0\\0&1&0&0\\0&0&1&0\\0&0&0&1\end{bmatrix}$	100	(2,1)	$\begin{bmatrix}1&0\\0&1\end{bmatrix}$	$\begin{bmatrix}1&0\\0&1\end{bmatrix}$	$\begin{bmatrix}0&0&1&0\\0&0&0&1\\1&0&0&0\\0&1&0&0\end{bmatrix}$
001	(1,2)	$\begin{bmatrix}1&0\\0&1\end{bmatrix}$	$\begin{bmatrix}0&1\\1&0\end{bmatrix}$	$\begin{bmatrix}1&0&0&0\\0&1&0&0\\0&0&0&1\\0&0&1&0\end{bmatrix}$	101	(2,1)	$\begin{bmatrix}1&0\\0&1\end{bmatrix}$	$\begin{bmatrix}0&1\\1&0\end{bmatrix}$	$\begin{bmatrix}0&0&0&1\\0&0&1&0\\1&0&0&0\\0&1&0&0\end{bmatrix}$
010	(1,2)	$\begin{bmatrix}0&1\\1&0\end{bmatrix}$	$\begin{bmatrix}1&0\\0&1\end{bmatrix}$	$\begin{bmatrix}0&1&0&0\\1&0&0&0\\0&0&1&0\\0&0&0&1\end{bmatrix}$	110	(2,1)	$\begin{bmatrix}0&1\\1&0\end{bmatrix}$	$\begin{bmatrix}1&0\\0&1\end{bmatrix}$	$\begin{bmatrix}0&0&1&0\\0&0&0&1\\0&1&0&0\\1&0&0&0\end{bmatrix}$
011	(1,2)	$\begin{bmatrix}0&1\\1&0\end{bmatrix}$	$\begin{bmatrix}0&1\\1&0\end{bmatrix}$	$\begin{bmatrix}0&1&0&0\\1&0&0&0\\0&0&0&1\\0&0&1&0\end{bmatrix}$	111	(2,1)	$\begin{bmatrix}0&1\\1&0\end{bmatrix}$	$\begin{bmatrix}0&1\\1&0\end{bmatrix}$	$\begin{bmatrix}0&0&0&1\\0&0&1&0\\0&1&0&0\\1&0&0&0\end{bmatrix}$

DOSM-PPM scheme with $n_t = 2$ and $L = 2$, in which there are two space-time mapping blocks: $\mathbf{X} = \begin{bmatrix}\mathbf{\Lambda}_1 & \mathbf{O}\\ \mathbf{O} & \mathbf{\Lambda}_2\end{bmatrix}$ and $\mathbf{X} = \begin{bmatrix}\mathbf{O} & \mathbf{\Lambda}_2\\ \mathbf{\Lambda}_1 & \mathbf{O}\end{bmatrix}$, each denoting index order of lasers in the spatial domain, where $\mathbf{O}$ is 2×2 zero matrix and $\mathbf{\Lambda}_k = \begin{bmatrix}\mathbf{x}_k\\ \mathbf{x}_k\mathbf{\Omega}\end{bmatrix}$, $k = (1,2)$ is the signal constellation on the corresponding laser at the k'th symbol period. $\mathbf{x}_k \in A$, $A = \{[1\quad 0], [0\quad 1]\}$ is the 2-PPM constellation (0 denotes that there is no light pulse at the corresponding position and 1 denotes that there is light pulse at the corresponding position). $\mathbf{\Omega} = \begin{bmatrix}0&1\\1&0\end{bmatrix}$ is 2×2 cyclic permutation matrix. Dimensions of $\mathbf{\Lambda}_k$ and $\mathbf{\Omega}$ are determined by the order of PPM. Easy to verify, $\mathbf{x}_k \in A$, $\mathbf{x}_k\mathbf{\Omega} \in A$, where $\mathbf{x}_k\mathbf{\Omega}$ denotes the signal inversion of $\mathbf{x}_k$, thus the differential process of the symbol domain on each laser is achieved. All of the space-time mapping matrix $\mathbf{X}$ of the DOSM scheme with $n_t = 2$ and 2-PPM is shown in Table 1.

2.3 *Differential Detection*

In the DOSM-PPM scheme transmission process, the received signal at t'th transmission block can be expressed as

$$\mathbf{Y}_t = \eta\sqrt{\mathcal{P}}\mathbf{H}_t\mathbf{S}_t + \mathbf{N}_t, \tag{2}$$

where η is photoelectric conversion efficiency, $\mathcal{P}$ is the average light power. For L-PPM constellation, a symbol period of length T_s is divided into L slots, each of length $T = T_s/L$. Assume that the received optical energy per symbol $E_s = \mathcal{P}T = \mathcal{P}T_s/L$ is a constant, the average light power is $\mathcal{P} = E_sL/T_s$. $\mathbf{N}_t$ denotes an $n_r \times (n_tL)$ real-valued matrix, each element of which is additive white Gaussian noise with zero mean and variance σ^2. $\mathbf{H}_t$ is $n_r \times n_t$ fading channel matrix, each element of which is independent and identically distributed (IID). Channel fading coefficient h obeys log-normal distribution of weak AT, and PDF is

$$f_{\mathbf{H}}(h) = \frac{1}{h\sigma\sqrt{2\pi}}\exp\left[-\frac{(\log_2 h - \mu)^2}{2\sigma^2}\right], \tag{3}$$

where mean and variance of h are $\mu = -\log_2(1+\sigma_{\mathrm{SI}}^2)$ and $\sigma^2 = \log_2(1+\sigma_{\mathrm{SI}}^2)$,[10] respectively. σ_{SI}^2 denotes the scintillation index. Similarly, the received signal at $(t-1)$'th transmission block can be written as

$$\mathbf{Y}_{t-1} = \eta\sqrt{\mathcal{P}}\mathbf{H}_{t-1}\mathbf{S}_{t-1} + \mathbf{N}_{t-1}. \tag{4}$$

The actual atmospheric environment is seen as the quasistatic channel. We can assume that its fading coefficients remain constant between adjacent transmitted matrices, i.e., $\mathbf{H}_t = \mathbf{H}_{t-1}$. Considering this fact and substituting Eqs. (1) and (4) into Eq. (2):

$$\mathbf{Y}_t = \mathbf{Y}_{t-1}\mathbf{X}_t - \mathbf{N}_{t-1}\mathbf{X}_t + \mathbf{N}_t = \mathbf{Y}_{t-1}\mathbf{X}_t + \hat{\mathbf{N}}_t, \tag{5}$$

where $\hat{\mathbf{N}}_t = \mathbf{N}_t - \mathbf{N}_{t-1}\mathbf{X}_t$. Therefore, the optimal MLSD can be derived as

$$\hat{\mathbf{X}}_t = \arg \min_{\forall \mathbf{X}_t \in \mathcal{X}} \|\mathbf{Y}_t - \mathbf{Y}_{t-1}\mathbf{X}_t\|_F^2, \tag{6}$$

where $\|\cdot\|_F^2$ is the Frobenius norm. Applying the $\text{trace}(\mathbf{AB}) = \text{trace}(\mathbf{BA})$, Eq. (6) can be simplified to

$$\hat{\mathbf{X}}_t = \arg \max_{\forall\, \mathbf{X}_t \in \mathcal{X}} \text{trace}(\mathbf{Y}_t^{\mathrm{T}}\mathbf{Y}_{t-1}\mathbf{X}_t), \tag{7}$$

where $\text{trace}(\cdot)$ is matrix trace operation. According to Eq. (7), the signal detecting at the Rx is obtained as is shown in Fig. 1. The estimated matrix $\hat{\mathbf{X}}_t$ is demodulated to the corresponding m bit sequence by means of MLSD.

3 Performance Analysis

In this section, the BER of DOSM-PPM is derived using the tight union-bound technique.[21] According to the union-upper bound theory, the BER can be expressed as

$$\text{BER} = \frac{1}{m2^m} \sum_{\mathbf{X}_l \in \mathcal{X}} \sum_{\hat{\mathbf{X}}_l \in \mathcal{X}} D(\mathbf{X}_l, \hat{\mathbf{X}}_l)\text{PEP}(\mathbf{X}_l, \hat{\mathbf{X}}_l|\mathbf{H}), \tag{8}$$

where $\mathbf{X}_l$ and $\hat{\mathbf{X}}_l$ denote all possible detected space-time mapping block at Rx side and estimated result, respectively. 2^m denotes all possible combinations of transmitted signal. $\text{PEP}(\mathbf{X}_l, \hat{\mathbf{X}}_l|\mathbf{H})$ denotes the pairwise error probability (PEP) of $\hat{\mathbf{X}}_l$ when it is detected given that $\mathbf{X}_l$ is actually transmitted. $D(\mathbf{X}_l, \hat{\mathbf{X}}_l)$ is the Hamming distance between the corresponding bit blocks of $\mathbf{X}_l$ and $\hat{\mathbf{X}}_l$. The number of PEP items increases with higher PPM orders and the number of lasers, leading to an increase in computational complexity. In order to simplify calculations, we choose $n_t = 2$, $L = 2$ DOSM system. The PEP for a given $\mathbf{H}$ can be formulated as follows:

$$\text{PEP}(\mathbf{X}_l \to \hat{\mathbf{X}}_l|\mathbf{H}) = \Pr(\|\mathbf{Y}_t - \mathbf{Y}_{t-1}\mathbf{X}_l\|_F^2 > \|\mathbf{Y}_t - \mathbf{Y}_{t-1}\hat{\mathbf{X}}_l\|_F^2), \tag{9}$$

which can be further simplified as

$$\text{PEP}(\mathbf{X}_l \to \hat{\mathbf{X}}_l|\mathbf{H}) = \Pr[(\mathbf{N}_t - \mathbf{N}_{t-1}\mathbf{X}_l)_F^2 > \|\mathbf{G} + \mathbf{N}_t - \mathbf{N}_{t-1}\hat{\mathbf{X}}_l\|_F^2], \tag{10}$$

where $\mathbf{G} = \eta\mathbf{H}_t\mathbf{S}_{t-1}(\mathbf{X}_l - \hat{\mathbf{X}}_l)$. Manipulate the right side of Eq. (10):

$$\|\mathbf{N}_t - \mathbf{N}_{t-1}\mathbf{X}_l\|_F^2 = \|\mathbf{N}_t\|_F^2 - 2\text{trace}\{\mathbf{N}_t^{\mathrm{T}}\mathbf{N}_{t-1}\mathbf{X}_l\} + \|\mathbf{N}_{t-1}\mathbf{X}_l\|_F^2, \tag{11}$$

$$\begin{aligned}\|\mathbf{G} + \mathbf{N}_t - \mathbf{N}_{t-1}\hat{\mathbf{X}}_l\|_F^2 &= \|\mathbf{G}\|_F^2 + 2\text{trace}\{\mathbf{G}^{\mathrm{T}}(\mathbf{N}_t - \mathbf{N}_{t-1}\hat{\mathbf{X}}_l)\} \\ &+ \|\mathbf{N}_t\|_F^2 - 2\text{trace}\{\mathbf{N}_t^{\mathrm{T}}\mathbf{N}_{t-1}\hat{\mathbf{X}}_l\} + \|\mathbf{N}_{t-1}\hat{\mathbf{X}}_l\|\|_F^2.\end{aligned} \tag{12}$$

Based on $\mathbf{X}_l\mathbf{X}_l^{\mathrm{T}} = \hat{\mathbf{X}}_l\hat{\mathbf{X}}_l^{\mathrm{T}} = \mathbf{I}$, $\|\mathbf{N}_t\mathbf{X}_l\|_F^2 = \|\mathbf{N}_{t-1}\hat{\mathbf{X}}_l\|_F^2$. Eq. (10) is rewritten as

$$\mathrm{PEP}(\mathbf{X}_l \to \hat{\mathbf{X}}_l|\mathbf{H}) = \Pr\{2\mathrm{trace}\{\mathbf{G}^{\mathrm{T}}(\mathbf{N}_t - \mathbf{N}_{t-1}\hat{\mathbf{X}}_l) - \mathbf{N}_t^{\mathrm{T}}\mathbf{N}_{t-1}(\hat{\mathbf{X}}_l - \mathbf{X}_l)\} > \|\mathbf{G}\|_F^2\}. \tag{13}$$

Notice that $\mathbf{N}_t$ and $\mathbf{N}_{t-1}$ are the Gaussian random variables (RVs) with zero mean and σ^2 variance. Consequently, as signal-to-noise ratio (SNR) increases, variance of $\mathbf{N}_t^{\mathrm{T}}\mathbf{N}_{t-1}$ approaches zero. Based on this approximation, Eq. (13) can be rewritten as

$$\mathrm{PEP}(\mathbf{X}_l \to \hat{\mathbf{X}}_l|\mathbf{H}) \approx \Pr\{\mathrm{trace}\{2\mathbf{G}^{\mathrm{T}}(\mathbf{N}_t - \mathbf{N}_{t-1}\hat{\mathbf{X}}_l)\} > \|\mathbf{G}\|_F^2\}. \tag{14}$$

Define $\Delta = \mathrm{trace}\{2\mathbf{G}^{\mathrm{T}}(\mathbf{N}_t - \mathbf{N}_{t-1}\hat{\mathbf{X}}_l)\}$. Δ obeys Gaussian RV with $E(\Delta) = 0$ and $\mathrm{Var}(\Delta) = 4\|\mathbf{G}^{\mathrm{T}}\|_F^2\sigma^2$, where $E(\cdot)$ and $\mathrm{Var}(\cdot)$ represent the expectation and variance, respectively. Therefore, we can get

$$\mathrm{PEP}(\mathbf{X}_l \to \mathbf{X}_k|\mathbf{H}) \approx Q\left(\frac{\|\mathbf{G}\|_F}{\sqrt{4\sigma^2}}\right), \tag{15}$$

where $Q(\cdot)$ is Gaussian Q-function. Using Craig's formulation of Q-function, namely

$$Q(x) = \frac{1}{\pi}\int_0^{\pi/2} \exp\left(-\frac{x^2}{2\sin^2\theta}\right)\mathrm{d}\theta. \tag{16}$$

Then the PEP of Eq. (16) can be rewritten as

$$\mathrm{PEP} = \frac{1}{\pi}\int_0^{\pi/2} M_\xi\left(-\frac{\rho\|\mathbf{G}\|_F^2}{2\sin^2\theta}\right)\mathrm{d}\theta, \tag{17}$$

where $M_\xi(\tau) = \int_0^\infty f_\xi(\Gamma)e^{\Gamma\tau}\mathrm{d}\Gamma$ is the moment generating function (MGF) of the RVs and $\rho = \frac{1}{4\sigma^2}$ is the SNR per symbol at Rx side. Taking the expectation of both sides of Eq. (17), average PEP (APEP) is obtained

$$\mathrm{APEP} = \frac{1}{\pi}\int_0^{\pi/2} E\left[M_\xi\left(-\frac{\rho\|\mathbf{G}\|_F^2}{2\sin^2\theta}\right)\right]\mathrm{d}\theta. \tag{18}$$

Because APEP cannot be directly obtained by Eq. (18), it is essential to get APEP upper bound by discussing error types of $\|\mathbf{G}\|_F^2$. Therefore, assume that $\hat{\mathbf{S}}_{t-1}$ is correctly detected, the analysis of $\|\mathbf{G}\|_F^2$ derives seven distinct error types as follows:

(1) E1: $\mathbf{X}_l = [\backslash]$, $\hat{\mathbf{X}}_l = [\backslash]$, $\mathbf{\Lambda}_{l1} = \hat{\mathbf{\Lambda}}_{l1}$, $\mathbf{\Lambda}_{l2} \neq \hat{\mathbf{\Lambda}}_{l2}$;
(2) E2: $\mathbf{X}_l = [\backslash]$, $\hat{\mathbf{X}}_l = [\backslash]$, $\mathbf{\Lambda}_{l1} \neq \hat{\mathbf{\Lambda}}_{l1}$, $\mathbf{\Lambda}_{l2} = \hat{\mathbf{\Lambda}}_{l2}$;
(3) E3: $\mathbf{X}_l = [\backslash]$, $\hat{\mathbf{X}}_l = [\backslash]$, $\mathbf{\Lambda}_{l1} \neq \hat{\mathbf{\Lambda}}_{l1}$, $\mathbf{\Lambda}_{l2} \neq \hat{\mathbf{\Lambda}}_{l2}$;
(4) E4: $\mathbf{X}_l = [\backslash]$, $\hat{\mathbf{X}}_l = [/]$, $\mathbf{\Lambda}_{l1} \neq \hat{\mathbf{\Lambda}}_{l1}$, $\mathbf{\Lambda}_{l2} = \hat{\mathbf{\Lambda}}_{l2}$;
(5) E5: $\mathbf{X}_l = [\backslash]$, $\hat{\mathbf{X}}_l = [/]$, $\mathbf{\Lambda}_{l1} = \hat{\mathbf{\Lambda}}_{l1}$, $\mathbf{\Lambda}_{l2} \neq \hat{\mathbf{\Lambda}}_{l2}$;
(6) E6: $\mathbf{X}_l = [\backslash]$, $\hat{\mathbf{X}}_l = [/]$, $\mathbf{\Lambda}_{l1} \neq \hat{\mathbf{\Lambda}}_{l1}$, $\mathbf{\Lambda}_{l2} \neq \hat{\mathbf{\Lambda}}_{l2}$;
(7) E7: $\mathbf{X}_l = [\backslash]$, $\hat{\mathbf{X}}_l = [/]$, $\mathbf{\Lambda}_{l1} = \hat{\mathbf{\Lambda}}_{l1}$, $\mathbf{\Lambda}_{l2} = \hat{\mathbf{\Lambda}}_{l2}$.

$[\backslash]$ and $[/]$ indicate a diagonal matrix and an antidiagonal matrix of laser index order, respectively. Simplify and classify the above seven error types:

$$\mathrm{APEP}_{\mathrm{E1}}(\mathbf{X}_l \to \hat{\mathbf{X}}_l) = \mathrm{APEP}_{\mathrm{E2}}(\mathbf{X}_l \to \hat{\mathbf{X}}_l) = E\left[Q\left(\sqrt{2\rho_1\mathbf{h}_1^{\mathrm{T}}\mathbf{h}_1}\right)\right], \tag{19}$$

$$\mathrm{APEP}_{\mathrm{E3}}(\mathbf{X}_l \to \hat{\mathbf{X}}_l) = \mathrm{PEP}_{\mathrm{E6}}(\mathbf{X}_l \to \hat{\mathbf{X}}_l) = E\left\{Q\left[\sqrt{2\rho_1(\mathbf{h}_1^{\mathrm{T}}\mathbf{h}_1 + \mathbf{h}_2^{\mathrm{T}}\mathbf{h}_2)}\right]\right\}, \tag{20}$$

$$\mathrm{APEP}_{\mathrm{E4}}(\mathbf{X}_l \to \hat{\mathbf{X}}_l) = \mathrm{PEP}_{\mathrm{E5}}(\mathbf{X}_l \to \hat{\mathbf{X}}_l) = E\left\{Q\left[\sqrt{\rho_1(\mathbf{h}_1^{\mathrm{T}}\mathbf{h}_1 + \mathbf{h}_2^{\mathrm{T}}\mathbf{h}_2 + \|\mathbf{h}_1 - \mathbf{h}_2\|_F^2)}\right]\right\}, \tag{21}$$

$$\mathrm{APEP}_{\mathrm{E7}}(\mathbf{X}_l \to \hat{\mathbf{X}}_l) = E\left[Q\left(\sqrt{2\rho_1\|\mathbf{h}_1 - \mathbf{h}_2\|_F^2}\right)\right], \tag{22}$$

where $\rho_1 = \eta^2\rho^2\mathcal{P}$ and $\mathbf{H} = [\mathbf{h}_1, \mathbf{h}_2]$. It can be seen from Eqs. (19)–(22) that the PDFs of $V_1 = 2\mathbf{h}_1^{\mathrm{T}}\mathbf{h}_1$, $V_2 = 2(\mathbf{h}_1^{\mathrm{T}}\mathbf{h}_1 + \mathbf{h}_2^{\mathrm{T}}\mathbf{h}_2)$, $V_3 = \mathbf{h}_1^{\mathrm{T}}\mathbf{h}_1 + \mathbf{h}_2^{\mathrm{T}}\mathbf{h}_2 + \|\mathbf{h}_1 - \mathbf{h}_2\|_F^2$, and $V_4 = 2\|\mathbf{h}_1 - \mathbf{h}_2\|_F^2$ are required to obtain the APEP of each error type.

We express V_1 and V_2 as $V_j = \sum_{i=1}^{q} c_i h_i^2$ $(j = 1, 2)$, where V_j also is a log-normal RV, c_i are the constants, h_i is IID log-normal RV, and q is the number of IID RVs. Mean μ_{V_j} and variance $\sigma_{V_j}^2$ of V_j are

$$\mu_{V_j} = n_r \exp(2\mu + 2\sigma^2)(c_1 + c_2), \tag{23}$$

$$\sigma_{V_j}^2 = n_r[\exp(4\sigma^2) - 1]\exp(4\mu + 4\sigma^2)(c_1^2 + c_2^2). \tag{24}$$

Closed-form expressions for the PDFs of the log-normal sum are not available, but the sum of squared log-normal RVs is approximated as $V_j = \sum_{i=1}^{q} c_i h_i^2 \approx e^{U_j}$, where U_j is a normal distribution RV with mean $\mu_{U_j} = \log(\mu_{V_j}/\sqrt{1 + \frac{\sigma_{V_j}^2}{\mu_{V_j}^2}})$ and $\sigma_{U_j}^2 = \log(1 + \frac{\sigma_{V_j}^2}{\mu_{V_j}^2})$, and the PDF of V_j are expressed as

$$f_{V_j}(v) = \frac{1}{\sqrt{2\pi}\sigma_{U_j}} \exp\left[-\frac{(\log v - \mu_{U_j})^2}{2\sigma_{U_j}^2}\right]. \tag{25}$$

As the result, the approximate MGF of sum of log-normal RVs can be written as

$$M_{\xi}(\tau) = \int_0^{\infty} \exp(\tau\xi)\frac{1}{\xi\sigma_{U_j}\sqrt{2\pi}}\left[-\frac{(\log \xi - \mu_{U_j})^2}{2\sigma_{U_j}^2}\right]\mathrm{d}\xi. \tag{26}$$

Equation (26) not has closed-form expression, but it can be approximated by the Gauss–Hermite expansion.[10] Therefore, MGF expression of RVs V_j can be rewritten as

$$M_{\xi}(\tau) \approx \sum_{n=1}^{\gamma} \frac{\omega_n}{\sqrt{\pi}} \exp\left[\tau \exp\left(\sqrt{2}\sigma_{U_j}a_n + \mu_{U_j}\right)\right], \tag{27}$$

where ω_n and a_n are the weight and abscissa factors for Gauss–Hermite integration,[10,31] and γ represents the number of terms used in the expansion. On substituting Eq. (27) into Eq. (19), the APEP of E1 and E2, E3, and E6 can be written as

$$\mathrm{APEP}_{\mathrm{E1,E2}} \approx \sum_{i=1}^{\gamma} \frac{\omega_n}{\sqrt{\pi}} Q\left(\sqrt{\rho_1 e^{\sqrt{2}\sigma_{U_1}a_n + \mu_{U_1}}}\right), \tag{28}$$

$$\mathrm{APEP}_{\mathrm{E3,E6}} \approx \sum_{i=1}^{\gamma} \frac{\omega_n}{\sqrt{\pi}} Q\left(\sqrt{\rho_1 e^{\sqrt{2}\sigma_{U_2}a_n + \mu_{U_2}}}\right). \tag{29}$$

For RV $V_3 = \mathbf{h}_1^{\mathrm{T}}\mathbf{h}_1 + \mathbf{h}_2^{\mathrm{T}}\mathbf{h}_2 + \|\mathbf{h}_1 - \mathbf{h}_2\|_F^2$ of E4 and E5, V_3 is approximated as $\mathbf{h}_1^{\mathrm{T}}\mathbf{h}_1 + \mathbf{h}_2^{\mathrm{T}}\mathbf{h}_2 + \|\mathbf{h}_1 - \mathbf{h}_2\|_F^2 \le 2(\mathbf{h}_1^{\mathrm{T}}\mathbf{h}_1 + \mathbf{h}_2^{\mathrm{T}}\mathbf{h}_2)$ using Cauchy inequality. Similarly, APEP of E4 and E5 can be written as

$$\mathrm{APEP}_{\mathrm{E4,E5}} \approx \sum_{i=1}^{\gamma} \frac{\omega_n}{\sqrt{\pi}} Q\left(\sqrt{\rho_1 e^{\sqrt{2}\sigma_{U3}a_n + \mu_{U_3}}}\right). \tag{30}$$

For RV $V_4 = 2\|\mathbf{h}_1 - \mathbf{h}_2\|_F^2$ of E7, although the linear combinations of log-normal can be described by an approximate log-normal distribution, the closed-form distribution of weighted

difference squares of two log-normal RVs do not exist. The APEP of E7 is not approximated using Gauss–Hermite integration. Therefore, using the Gauss kernel density estimation method,[10] APEP for RV V_4 can be approximated as

$$\mathrm{APEP}_{\mathrm{E7}} \approx \sum_{i=1}^{\alpha} \frac{1}{\alpha\pi} \int_0^{\pi/2} M_{K_i}\left(-\frac{\rho_1}{2\sin^2\theta}\right) \mathrm{d}\theta, \tag{31}$$

where α stands for a kernel size and $M_{K_i}(\tau) = \exp(\mu_{\mathrm{KDE}}\tau + \frac{1}{2}b^2\tau^2)$, μ_{KDE} and b are the mean of Gaussian distributed variables and kernel estimator bandwidth, respectively.

Substituting Eqs. (28)–(31) into Eq. (8) and calculating the Hamming distance of each type error, the ABER upper bound of $2 \times n_r$ DOSM-2PPM in the weak turbulent channel can be rewritten as

$$\mathrm{ABER} \leq \frac{2}{3}(\mathrm{APEP}_{\mathrm{E1,E2}} + \mathrm{APEP}_{\mathrm{E3}}) + \frac{4}{3}\mathrm{APEP}_{\mathrm{E4,E5}} + \mathrm{APEP}_{\mathrm{E6}} + \frac{1}{3}\mathrm{APEP}_{\mathrm{E7}}. \tag{32}$$

4 Simulation and Analysis

In this section, the BER performance of the proposed DOSM with L-PPM scheme under log-normal fading channel is analyzed by means of Monte Carlo simulation and is compared with different OSM schemes,[10] such as SPPM scheme, well known differential schemes,[25] such as DOSSK scheme and DOSM-PAM scheme. Consider that the CSI is perfectly known at the Rx of the OSM scheme, and the MLSD detection is used to all schemes. The x axis of all figures represents per symbol SNR. In order to facilitate the description (n_t, n_r) are used to label the parameters of DOSM system. All system simulation parameters are given in Table 2.

For a DOSM scheme with L-PPM, n_t lasers construct an orthogonal space-time block, so $\lfloor \log_2(n_t!) \rfloor$ bits are transmitted by selecting lasers index order in spatial domain, whereas $n_t \log_2(L)$ bits are mapped on n_t activated lasers using multiplex technology. Each activated laser transmits different PPM signals. Therefore, the transmission rate is $\lfloor \log_2(n_t!) \rfloor + n_t \log_2(L)$ bit per channel use (bpcu), and the SE on continuous $n_t L$ slots can be expressed as $R_{\mathrm{DOSM,L\text{-}PPM}} = \frac{\log_2(n_t!) + n_t \log_2 L}{n_t L}$ (bits/s/Hz). The transmission rate and SE are given in Table 3. It is shown that the number of lasers and PPM order are two important factors affecting the transmission rate and SE of the DOSM scheme. The transmission rate increases with increasing number of n_t and L. Note that the use of multiplex technology has a significant improvement on transmission rate. The SE is determined by the specific value of n_t and L. But since bandwidth is not limited in WOC system, SE is not considered as an important element.

Table 2 System parameters.

Parameter	Symbol	Value
Wavelength	λ	1550 nm
Receiver radius	r	25 cm
Link distance	l	1000 m
Refractive-index structure parameter	C_n^2	3.0×10^{-14}
Beam waist radius	w_0	2 cm
Phase front radius	F_0	−10 m
Photoelectric conversion efficiency	η	0.5
SI	σ_{SI}^2	0.6
Kernel estimator bandwidth	b	1/5000

Table 3 Comparison of SE and transmission rate of different schemes.

Modulation	SE (bit/s/Hz)	Transmission rate (bpcu)
DOSM-PPM	$\frac{\lfloor \log_2(n_t!) \rfloor + n_t \log_2 L}{n_t L}$	$\lfloor \log_2(n_t!) \rfloor + n_t \log_2 L$
DOSM-PAM	$\frac{\lfloor \log_2(n_t!) \rfloor + \log_2 \mathcal{M}}{n_t}$	$\lfloor \log_2(n_t!) \rfloor + \log_2 \mathcal{M}$
DOSSK	$\frac{\lfloor \log_2(n_t!) \rfloor}{n_t}$	$\lfloor \log_2(n_t!) \rfloor$
SPPM	$\frac{\log_2(n_t L)}{L}$	$\log_2(n_t L)$

Figure 2 shows simulation and theoretical BER curves of (2,3) and (2,4) DOSM-2PPM schemes for log-normal fading channels. It can be observed that theoretical performance curves are in agreement with the simulation results at high SNR values. For (2,3) DOSM-2PPM scheme, at BER $\leq$ 24 dB, the theoretical BER curve is higher than the simulation curve, and when the SNR $\geq$ 24 dB, the simulation BER curve coincides with theoretical curve. Due to the use of upper-bound technique to derive BER, the theoretical BER is asymptotically tight with the increase of SNR.[23] Therefore, in the low SNR range, the theoretical calculation results are higher than the actual ones due to the large noise power.

Figure 3 shows BER curves, transmission rate, and SE of different DOSM-PPM schemes. First, it can be observed from (2,3) DOSM-2PPM, DOSM-4PPM, and DOSM-8PPM, the SNR of DOSM-8PPM scheme performs 2.5 dB better than that of the DOSM-4PPM at 1×10^{-3} BER, and DOSM-4PPM scheme is shown to outperform DOSM-2PPM by 3 dB at 1×10^{-3} BER. In

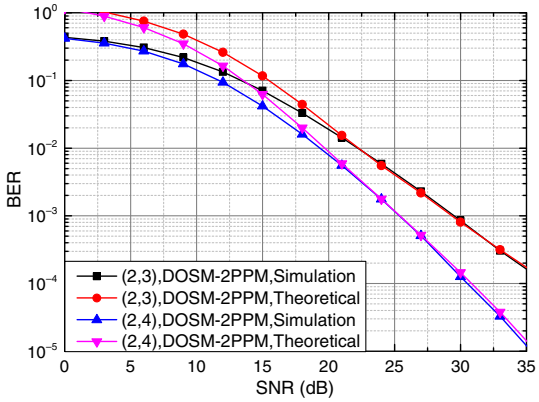

Fig. 2 Theoretical BER and simulation BER of the $n_t = 2$ DOSM-2PPM scheme.

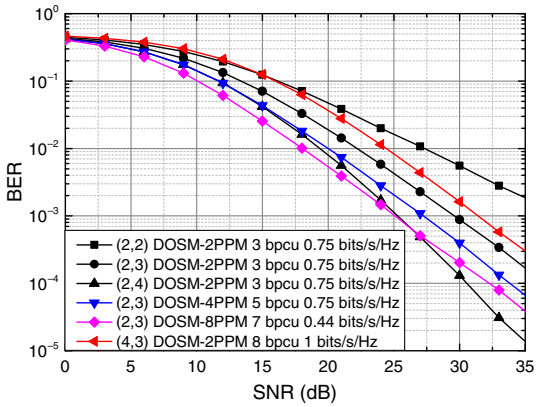

Fig. 3 BER curves of different DOSM-PPM schemes.

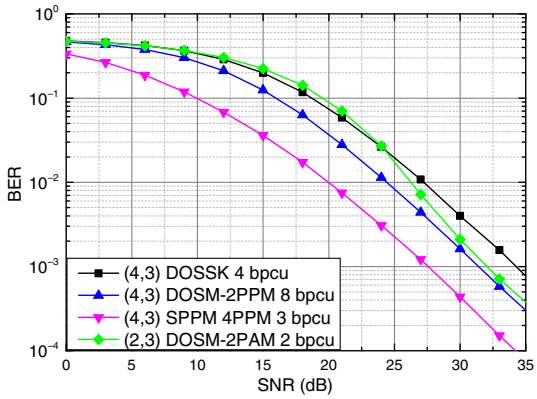

Fig. 4 BER curves of different schemes at 1 bits/s/Hz.

addition, the SE of the DOSM-2PPM scheme is 0.75 bits/s/Hz, whereas for DOSM-4PPM scheme and DOSM-8PPM scheme, SE is 0.71 and 0.44 bits/s/Hz, respectively. When the PPM order is increased under the same number of lasers, the BER performance of the proposed DOSM-PPM scheme is improved at the cost of SE. Second, it can be seen from (2,3) DOSM-2PPM and (4,3) DOSM-2PPM scheme, the SNR of (2,3) DOSM scheme performs 2 dB better than that of the (4,3) DOSM scheme at 1×10^{-3} BER. What is more, when the number of lasers increases from 2 to 4, SE and transmission rate of DOSM-PPM scheme increase from 0.75 to 1 bits/s/Hz, 3 to 8 bpcu, respectively. Therefore, when n_t increases on each activated laser with the same order PPM, transmission rate of the DOSM-PPM scheme increases at the cost of the BER loss. Third, diversity order δ can be obtained by calculating the slope at very high SNR. For example, BER for $n_r = 2$ DOSM scheme is 1.8×10^{-2} at 25 dB, whereas it is 1.1×10^{-2} at 35 dB, which leads to $\delta = \log[1.1 \times 10^{-3}/(1.1 \times 10^{-2})] \approx 1.0$. The diversity order will turn out to be $n_r/2$.[25]

Figure 4 shows the BER curves of proposed DOSM scheme and other OSM schemes at the same SE of 1 bits/s/Hz, such as SPPM, DOSSK, and DOSM-PAM schemes. In order to achieve 1 bits/s/Hz, we choose (4,3) SPPM with 4-PPM scheme and (4,3) DOSSK scheme. In DOSM-PAM scheme of Table 3, $\mathcal{M}$ is the PAM order, and all activated lasers transmit the same PAM signal. Amplitude values of 2-PAM is 0.75 and 1.25. It can be observed from Fig. 4 DOSM-PPM scheme outperforms DOSM-PAM and DOSSK schemes by 1 and 3 dB at 1×10^{-3} BER, respectively. The DOSM-2PPM scheme performs 4 dB less than SPPM with 4-PPM scheme at 1×10^{-3} BER, which requires the accurate CSI. It is perfectly reasonable to avoid CSI estimation with a loss of <4 dB. What is more, the transmission rate and SE of several different schemes are given in Table 3. With the same 1 bits/s/Hz SE, the transmission rates of DOSM-PPM, SPPM, DOSSK, and DOSM-PAM scheme are 8, 4, 4, and 2 bpcu, respectively.

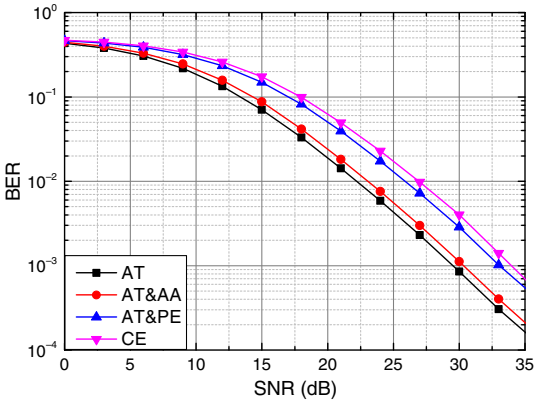

Fig. 5 Error performance of different effect factors for DOSM-2PPM scheme.

Therefore, our proposed DOSM-PPM scheme obtains higher transmission rate compared with other schemes.

In addition to AT, PE, and atmospheric attenuation (AA) are also important factors affecting error performance in WOC system. The combined effect (CE) includes AT, PE, and AA. The channel characteristic matrix under the CE is $h = h^a h^p h^l$.[32] h^a denotes AT, $h^p \approx A_0 e^{-2R^2/w^2}$ denotes PE,[33] where A_0 is the equivalent receiver area, w is the equivalent beam waist at Rx, and R^2 is the radial distance.[33] $h^l = e^{-\sigma_z l}$ denotes AA, where σ_z is the attenuation coefficient. When $l = 1000$ m, $h^l = 0.9$.[32] Error performances of different effect factors in DOSM-2PPM system are given in Fig. 5. It can be observed from Fig. 5, SNR of AT and AA degrades 0.5 dB compared with system of AT at BER $= 10^{-3}$. SNR of AT and PE degrades 6 dB compared with system of AT at BER $= 10^{-3}$. Therefore, the CE has a serious influence on the error performance, in which the influence of PE on the BER is greater than that of AA.

5 Conclusion

In this paper, we have proposed a DOSM-PPM scheme. By designing a special space-time mapping block, our proposed scheme achieves PPM's differential operation. Utilizing PPM on each activated laser optimizes DOSM system's performance. Taking $n_t = 2$ DOSM-2PPM scheme as an example, the theoretical BER performance is analyzed. Using Monte Carlo simulation, we discussed the effect of the number of lasers and the PPM order on BER, transmission rate, and SE, respectively. The proper selection of PPM order and number of lasers is to achieve the trade-off among BER, transmission rate, and power consumption. With the same SE, DOSM-PPM scheme improves the transmission rate and outperforms DOSM-PAM scheme by almost 1 dB at 1×10^{-3} BER. In our DOSM-PPM scheme, the adoption of MLSD decoding algorithm results in a high decoding complexity. So we optimize and explore some low complexity decoding and detection algorithms suitable for DOSM-PPM scheme in the following research.

Acknowledgments

This work was supported by the National Natural Science Foundation of China (No. 61861026). All the authors have no relevant financial interests in this manuscript and no other potential conflicts of interest to disclose in this manuscript.

References

1. H. S. Khallaf and H. M. H. Shalaby, "Closed form expressions for SER and capacity of shot noise limited MIMO-FSO system adopting MPPM over gamma–gamma atmospheric turbulence channels," in *IEEE Photonics Conf. (IPCon)*, San Diego, California, pp. 619–620 (2014).
2. H. S. Khallaf et al., "SER analysis of MPPM-Coded MIMO-FSO system over uncorrelated and correlated gamma–gamma atmospheric turbulence channels," *Opt Commun.* **356**, 530–535 (2015).
3. H. Wang et al., "Ergodic channel capacity of spatial correlated multiple-input multiple-output free space optical links using multipulse pulse-position modulation," *Opt. Eng.* **56**(2), 026103 (2017).
4. R. Mesleh et al., "Spatial modulation—a new low complexity spectral efficiency enhancing technique," in *1st Int. Conf. Commun. and Networking*, Beijing, pp. 1–5 (2006).
5. R. Mesleh et al., "Spatial modulation," *IEEE Trans. Veh. Technol.* **57**(4), 2228–2241 (2008).
6. R. Mesleh et al., "Indoor MIMO optical wireless communication using spatial modulation," in *IEEE Int. Conf. Commun. (ICC)*, Cape Town, pp. 1–5 (2010).
7. W. O. Popoola et al, "Spatial pulse position modulation for optical communications," *J. Lightwave Technol.* **30**(18), 2948–2954 (2012).

8. T. Fath et al., "Coded spatial modulation applied to optical wireless communications in indoor environments," in *IEEE Wireless Commun. and Networking Conf.*, Paris, pp. 1000–1004 (2012).
9. H. T. T. Pham et al., "Performance analysis of spatial PPM-based free-space optical communication systems with Gaussian beam," in *Int. Conf. Adv. Technol. for Commun. (ATC)*, Hanoi, pp. 144–148 (2014).
10. T. Özbilgin et al., "Optical spatial modulation over atmospheric turbulence channels," *IEEE/OSA J. Lightwave Technol.* **33**(11), 2313–2323 (2015).
11. M. Abaza et al., "The performance of space shift keying for free-space optical communications over turbulent channels," *Proc. SPIE* **9387**, 93870V (2015).
12. A. Jaiswal et al., "On the ergodic capacity of optical space shift keying based FSO-MIMO system under atmospheric turbulence," in *IEEE Int. Conf. Commun. (ICC)*, Paris, pp. 1–7 (2017).
13. A. Jaiswal et al., "BER analysis of optical space shift keying in atmospheric turbulence environment," in *10th Int. Symp. Commun. Syst., Networks and Digital Signal Proc. (CSNDSP)*, Prague, pp. 1–6 (2016).
14. A. Jaiswal et al., "Performance of optical space shift keying over gamma–gamma fading with pointing error," *IEEE Photonics J.* **9**(2), 1–16 (2017).
15. A. Jaiswal et al., "An investigation of performance and diversity property of optical space shift keying-based FSO-MIMO system," *IEEE Trans. Commun.* **66**(9), 4028–4042 (2018).
16. A. Jaiswal et al., "Partially informed transmitter-based optical space shift keying under atmospheric turbulence," *IEEE Trans. Wireless Commun.* **18**8), 3781–3796 (2019).
17. V. Tarokh and H. Jafarkhani, "A differential detection scheme for transmit diversity," in *IEEE Wireless Commun. and Networking Conf. (WCNC)*, New Orleans, Louisiana, Vol. 3, pp. 1043–1047 (1999).
18. S. Alamouti, "A simple transmit diversity technique for wireless communications," *IEEE J. Sel. Areas Commun.* **16**(8), 1451–1458 (1998).
19. Y. Bian, et al., "differential spatial modulation," *IEEE Trans. Veh. Technol.* **64**(7), 3262–3268 (2015).
20. M. Wen et al., "Performance analysis of differential spatial modulation with two transmit antennas," *IEEE Commun. Lett.* **18**(2), 476–477 (2014).
21. R. Mesleh et al., "Differential quadrature spatial modulation," *IEEE Trans. Commun.* **65**(9), 3810–3817 (2017).
22. T. P. Nguyen et al., "Differential spatial modulation for high-rate transmission systems," *EURASIP J. Wireless Commun. Networking* **2018**(1), 6 (2018)
23. J. Liu et al., "High-rate APSK aided differential spatial modulation: design method and performance analysis," *IEEE Commun. Lett.* **21**1), 168–171 (2017).
24. C. Wu et al, "Space-time block coded rectangular differential spatial modulation: system design and performance analysis," *IEEE Trans. Commun.* **67**(9), 6586–6597 (2019).
25. A. Jaiswal et al., "Differential optical spatial modulation over atmospheric turbulence," *IEEE J. Sel. Top. Signal Process.* **13**(6), 1417–1432 (2019).
26. F. Xu et al., "Coded PPM and multipulse PPM and iterative detection for free-space optical links," *IEEE/OSA J. Opt Commun. Networking* **1**(5), 404–415 (2009).
27. G. Xu, "BER and channel capacity of a deep space FSO communication system using L-PPM-MSK-SIM scheme during superior solar conjunction," *Opt. Express* **27**(17), 24610–24623 (2019).
28. L. Hughes, "Differential space-time modulation," *IEEE Trans. Inf. Theory* **46**(7), 2567–2578 (2000).
29. Z. Wang et al., "Performance comparison of different modulation formats over free-space optical (FSO) turbulence links with space diversity reception technique," *IEEE Photonics J.* **1**(6), 277–285 (2009).
30. G. Xu, "Error performance of deep space optical communication with M-ary pulse position modulation over coronal turbulence channels," *Opt. Express* **27**(9), 13344–13356 (2019).
31. "Nodes and Weights of Gauss–Hermite Calculator," (n.d.) http://keisan.casio.com/exec/system/1281195844 (accessed Feb. 2017).

32. A. Farid and S. Hranilovic, "Outage capacity optimization for free-space optical links with pointing errors," *J. Lightwave Technol.* **25**(7), 1702–1710 (2007).
33. A. Farid and S. Hranilovic, "Diversity gain and outage probability for MIMO free-space optical links with misalignment," *IEEE Trans. Commun.* **60**(2), 479–487, (2012).

Huiqin Wang received her BEng degree in communication engineering from Lanzhou Jiaotong University, Lanzhou, China, in 1996 and her PhD in microelectronics and solid-state electronics from Xi'an University of Technology, Xi'an, China, in 2011. Currently, she is a professor at the School of Computer and Communication of Lanzhou University of Technology. Her research interests include the theory and technology of wireless optical communications.

Yicong Mao received his BEng degree in communication engineering from the Lanzhou University of Technology, Lanzhou, China, in 2017, where he is currently pursuing his MEng degree in communication and information systems. His research interests include technology of wireless optical communications and optical MIMO technology.

Yue Zhang received her BS degree from Nanjing University of Posts and Telecommunications, Nanjing, China, in 2016. Currently, she is pursuing her PhD in manufacturing and information systems from the Lanzhou University of Technology, Lanzhou, China. Her research interests include technology of wireless optical communications and optical MIMO technology.

Minghua Cao received his BEng degree in communication engineering from Gansu University of Technology, Lanzhou, China, in 2002, MEng degree in signal and information processing from Lanzhou University of Technology, Lanzhou, China, in 2009, and his PhD in electronic science and technology from Beijing University of Posts and Telecommunications, Beijing, China, in 2016. His research interests include free space optical communication systems and low-cost radio-over-fiber networks.

Chanfei Wang received her PhD from Beijing University of Posts and Telecommunications (BUPT) in 2016. Her research focuses on signal processing for wireless communications.

Zhongxian Bao received her BEng degree in mechanical design and manufacturing automation from Lanzhou University of Technology, Lanzhou, China, in 1991 and her MEng degree in mechanical design and manufacturing automation from Lanzhou University of Technology in 1997. Her research focuses on application of computer technology.